

# Near-Surface Atmospheric Behavior over Complex Tropical Topography in Puerto Rico Dominated by Seasonal Patterns Despite Frequent Environmental Changes

ASHLEY E. VAN BEUSEKOM<sup>a</sup> AND GRIZELLE GONZÁLEZ<sup>a</sup>

<sup>a</sup> *International Institute of Tropical Forestry, U.S. Department of Agriculture Forest Service, Río Piedras, Puerto Rico*

(Manuscript received 14 September 2021, in final form 6 May 2022)

**ABSTRACT:** Understanding near-surface atmospheric behavior in the tropics is imperative given the role of tropical energy fluxes in Earth's climate cycles, but this area is complicated by a land–atmosphere interaction that includes rugged topography, seasonal weather drivers, and frequent environmental disturbances. This study examines variation in near-surface atmospheric behaviors in northeastern Puerto Rico using a synthesis of data from lowland and montane locations under different land covers (forest, urban, and rural) during 2008–21, when a severe drought, large hurricanes (Irma and Maria), and the COVID-19 mobility-reducing lockdown occurred. Ceilometer, weather, air quality, radiosonde, and satellite data were analyzed for annual patterns and monthly time series of data and data correlations. The results showed a system that is strongly dominated by easterly trade winds transmitting regional oceanic patterns over terrain. Environmental disturbances affected land–atmosphere interaction for short time periods after events. Events that reduce the land signature (reducing greenness: e.g., drought and hurricanes, or reducing land pollution: e.g., COVID-19 lockdown) were evidenced to strengthen the transmission of the oceanic pattern. The most variation in near-surface atmospheric behavior was seen in the mountainous areas that were influenced by both factors: trade winds, and terrain-induced orographic lifting. As an exception to the rest of the near-surface atmospheric behavior, pollutants other than ozone did not correlate positively or negatively with stronger trade winds at all sites across the region. Instead, these pollutants were hypothesized to be more anthropogenically influenced. Once COVID-19 lockdown had persisted for 3 months, urban pollution decreased and cloud base may have increased.

**KEYWORDS:** Tropics; Extreme events; Atmosphere–land interaction; Seasonal variability

## 1. Introduction

The energy fluxes in the tropics are understood to be very important part to Earth's climate cycle, but these fluxes are regulated by the less-well-understood interaction between tropical land and atmosphere (Gentine et al. 2019). Many tropical islands are mountainous, and the active and passive disruption of the atmosphere by mountains further complicates the system (thermal and radiative energy exchange when the diurnal cycle interacts with terrain vs momentum exchange when the atmospheric flow is modified by the presence of terrain; De Wekker and Kossmann 2015). The nature of the interaction will change with movement across the landscape from the coast inland, with changing characteristics of anthropogenic development and topography. Available moisture, temperature, and carbon all contribute to the land–atmosphere interaction. These variables change seasonally and can be altered by events (such as droughts, hurricanes, and lockdowns), which in turn affect the area differently depending on the land characteristics. The

question of how much such events can change the near-surface atmospheric behavior, and if there is a tipping point with more and more frequent events in the tropics, has long been discussed (e.g., Lawton et al. 2001).

The land–atmosphere interaction occurs in an area called the planetary boundary layer (PBL), which is more complicated in areas with rugged terrain. The mixing layer height (MLH) typically marked by strong gradients in aerosol concentration in the PBL (Eresmaa et al. 2006). Convective clouds form above the MLH and pollutants are mostly trapped inside the PBL. Orographic lifting over mountain topography forms clouds, and strong winds at mountains may raise the height of the MLH, making a thicker PBL and more diluted pollutants (Singh et al. 2016). In seasons with stronger winds, these effects may be more pronounced. On the other hand, ozone is a pollutant that comes from downward mixing from the stratosphere as well as anthropogenic sources, so ozone concentrations are greater at higher elevations (Vingarzan 2004), but behavior with wind depends on whether the wind brings more or fewer anthropogenic sources to an area. Beyond wind, cloud, and aerosol behavior and land surface conditions are subject to annual weather patterns. Feedbacks are also part of the system, as shallow clouds and aerosols affect change in local surface conditions (e.g., low cloud cover reduces temperature; Quan et al. 2013). Characterizing annual patterns of atmosphere and weather across a landscape with complex terrain is a first step in understanding land–atmosphere interaction in the tropics (Couach et al. 2003), with the next step being understanding event-causative variation.

Supplemental information related to this paper is available at the Journals Online website: <https://doi.org/10.1175/EI-D-21-0020.s1>.

Corresponding author: Ashley E. Van Beusekom, [avbscience@gmail.com](mailto:avbscience@gmail.com)

*Earth Interactions* is published jointly by the American Meteorological Society, the American Geophysical Union, and the Association of American Geographers.

DOI: 10.1175/EI-D-21-0020.1

For information regarding reuse of this content and general copyright information, consult the [AMS Copyright Policy \(www.ametsoc.org/PUBSReuseLicenses\)](https://www.ametsoc.org/PUBSReuseLicenses).

Since clouds regulate climate and bring rainfall, event-causative variation in cloud behavior has long been a topic of interest (Ramanathan et al. 1989). Shallow convection (nonprecipitating) clouds have a much shorter life-span than deep convective clouds and thus are more influenced by changes in local surface conditions (Gentine et al. 2019). A drought reduces evapotranspiration, theoretically raising cloud base and reducing cloud cover (Still et al. 1999). A hurricane results in defoliation, which may also raise cloud base and reduce cloud cover (Nair et al. 2003; Ray et al. 2006). Yet recent research suggest defoliation may reduce the local land influence on clouds, such that clouds follow regional oceanic patterns instead of being influenced by land heating (Miller et al. 2019). Drastic reductions in pollution are another possibility for raising cloud base and reducing cloud cover, as aerosols act as cloud condensation nuclei (Latha et al. 2021). Conversely, the increase of aerosols may inhibit cloud activity. Smoke can delay the onset of shallow cumulus cloud development (Barbaro et al. 2014). The presence of the Saharan air layer of dust-rich air suppresses convective cloud activity in the Caribbean (Mote et al. 2017). In an opposite causative manner, high convective clouds may scavenge the pollutant of mercury from the troposphere and deposit it in the tropics, so a lack of high clouds may reduce pollution (Shanley et al. 2020).

In this study, the near-surface atmospheric patterns are characterized over a path from ocean to montane cloud forest to large city, in northeastern Puerto Rico using 13.5 years (January 2008–May 2021) of cloud, aerosol, and weather data from five general locations including satellite tracks. This study does not include measurements of surface turbulent flux and associated momentum, energy, water, and trace gases exchanges between the land and the near-surface atmosphere; measurements that are required to characterize complex land–atmosphere interactions. The regional characteristics presented in this study can motivate collection and analysis of direct flux measurements; these measurements are necessarily local but currently needed to downscale regional remote sensing estimates of the land–atmosphere interactions (Brown and Lugo 2017; Gentine et al. 2019).

Three large environmental disturbances occurred over the area between 2008 and 2021. In summer 2015 a drought affected the island, starting in May 2015. The island was still experiencing drought conditions until March 2016 (using anthropogenic criteria to include agricultural soils and plants; <https://droughtmonitor.unl.edu>), although precipitation increased after September 2015. Satellite data showed a loss of 11% of greenness in the Luquillo Experimental Forest (LEF) during the drought (Schwartz et al. 2019). Next, on 7 September 2017, category-5 Hurricane Irma defoliated the northern belt of Puerto Rico and 13 days later category-4 Hurricane María made a direct hit on Puerto Rico, with 51% of the greenness lost in the LEF and 31% lost in Puerto Rico as a whole from these two events (Van Beusekom et al. 2018). Pollution was measurably increased in the capital in the months after the hurricanes, because of the use of generators (Subramanian et al. 2018). Then, on 15 March 2020, Puerto Rico started lockdowns to prevent the spread of the COVID-19 virus. The lockdowns were mostly continuous through 10 March 2021.

The lockdowns reduced anthropogenic sources of pollution, decreasing mobility outside residences in Puerto Rico by 65%–87% in the first month of lockdown, and still decreased by 7%–22% 4 months after lockdowns were over (<https://www.google.com/covid19/mobility/>). The composite dataset of cloud, aerosol, and weather data over complex terrain and a tumultuous decade provided an opportunity to study the variety in tropical near-surface atmospheric behavior, from seasonal patterns to possible changes, now and into the future.

## 2. Study area

The weather in northeastern Puerto Rico is dominated by the easterly trade winds, like much of the Caribbean Sea region (Malkus 1955; Odum and Pigeon 1970). The trade wind direction is slightly north ( $0^\circ$ ) of east ( $90^\circ$ ), at  $80^\circ$ – $90^\circ$  (Jury 2020). Annual trade winds are driven by an interplay of the North Atlantic subtropical high (NASH) sea level pressure system and the intertropical convergence zone (ITCZ) position (Giannini et al. 2000). In the Northern Hemisphere summer, the ITCZ moves to its northern position in the southwest Caribbean, weakening the trade winds. Weaker trade winds allow daytime confluence to increase and topography to gather and lift more moisture, as well as give way to the progression of tropical easterly low pressure waves ( $60^\circ$ – $110^\circ$ ), which help to create a Caribbean wet season April/May through November (Jury 2020). During winter, the NASH maxima over the subtropical Atlantic extends westward, strengthening the trade winds and suppressing convection to create a cooler dry season December through March (Gouirand et al. 2012), with rainfall from stratiform systems. The Caribbean low-level jet is a strengthening of the trade winds in June and July, separating the rain season into early and late with a warm drier season called the midsummer drought (Taylor et al. 2013). This strengthening of the trade winds also brings Saharan dust intrusions, which stabilize the atmosphere and may inhibit rainfall (Jury and Santiago 2010; Mote et al. 2017).

Pollution is relatively low in Puerto Rico due to the smaller population and the pollutant dispersion by the trade winds, but there is pollution from vehicle and generator use. Pollution in Puerto Rico is thought to contribute to clouds with higher droplet concentrations, and research suggests this pollution may be a bigger factor in cloud processes than the Saharan dust intrusions (Torres-Delgado et al. 2021). Broadly speaking, vehicles burning primarily gasoline produce more carbon monoxide (CO) than generators and ships, which burn primarily diesel and produce more nitrogen dioxide (NO<sub>2</sub>) and sulfur dioxide (SO<sub>2</sub>). Ground-level ozone is another pollutant, formed as a secondary pollutant from stratospheric ozone interacting with tropospheric nitrogen oxides (NO and NO<sub>2</sub>), but the nitrogen oxides can come from over the ocean (countries far to the east and ships) and tropospheric ozone is also collected from across the ocean with higher elevation areas collecting more (Erickson et al. 2020). Due to the chemistry of the reaction, in high nitrogen oxide areas such as cities, the more nitrogen oxide the more ozone is created, but if the nitrogen oxide

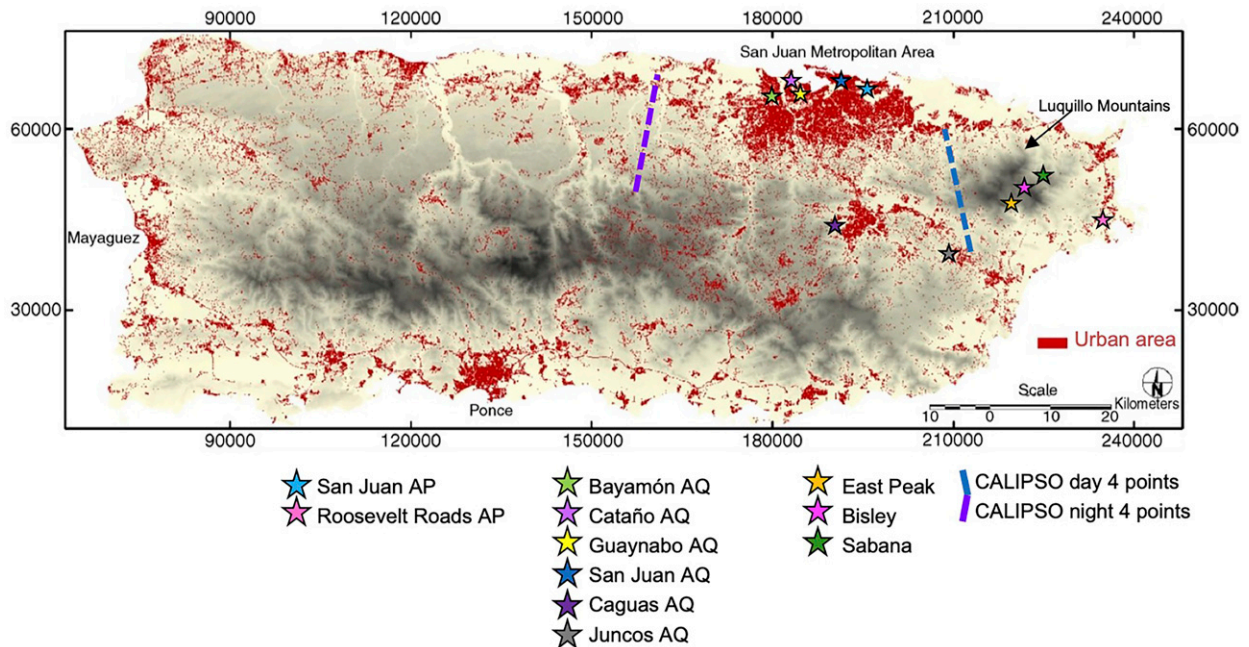


FIG. 1. Map of all locations of data collection, including dashed lines of satellite tracks. The background map of urban area and topography is from [Martinuzzi et al. \(2007\)](#). Here, AP indicates airport station and AQ indicates air quality station.

concentration is low enough, when nitrogen oxide decreases more ozone is created ([Wolff et al. 2013](#)).

In 2015, the median year of this study, 3.5 million people lived in Puerto Rico with more than one-third of the population living in the capital city, the San Juan metropolitan area (San Juan and its conurbation of the municipalities of Bayamón, Carolina, Cataño, Guaynabo, and Trujillo Alto, 2015 population 1.25 million; <https://www.census.gov/>). Island population declined at an increasing rate of 0.5–3.9% during the time of this study (2008–21). San Juan is in the coastal plains of the central northern coast of Puerto Rico, with the Luquillo Mountains in the path of the trade winds to the southeast, and more rural coastal plains eastward beyond that ([Fig. 1](#)).

In the Luquillo Mountains, most of the area is covered by the protected study site of the LEF ([Fig. 1](#)). Maximum elevation is 1077 m. High rainfall causes steep, dissected slopes and the ridges and stream valleys are covered by undeveloped tropical forest. The vegetation and the associated diurnal transpiration stimulate afternoon convection ([Malkus 1955](#)). Low clouds are seasonally invariant enough to create a cloud forest starting around 750 m ([Van Beusekom et al. 2017](#)). Low dry season clouds are thought to be the result of proximity to the stable oceanic cloud system ([Nuijens et al. 2014](#)); along with local trade wind orographic lifting and cloud formation. Based on measurements, aerosol sources in the forest are also thought to be mostly coming from over the ocean, with the addition of local natural sources but not much anthropogenic influence from the island ([Gioda et al. 2013](#)).

Elevational gradient analysis within northeast Puerto Rico, down from the Luquillo Mountain peaks to the coast and

inland to San Juan, show microclimate and soil influence with differing vegetation types ([Waide et al. 2013](#); [González et al. 2013](#); [Gould et al. 2006](#)). Temperature and precipitation have approximately linear relationships with elevation on average across the gradient ([Van Beusekom et al. 2015](#)). In the forest, productivity also varies strongly with elevation-dependent insolation, in comparison with other abiotic influences ([Wang et al. 2003](#)). However, Puerto Rico is a hurricane disturbance-mediated environment and elevation alone does not control environmental characteristics ([Willig et al. 2011](#)). Hurricane disturbance effects in any one area are strongly related to accessibility to wind, driven by storm tracks and moderated by topographic shading and vegetation characteristics ([Van Beusekom et al. 2018](#)). Larger mesoclimates have been distinguished: 1) the urban heat island around San Juan, 2) the Luquillo Mountains, and 3) the area to the southeast of the mountains ([Velazquez-Lozada et al. 2006](#)). Land–atmosphere data collected in each of these mesoclimates was used for this study.

### 3. Methods

This study used five kinds of data: ceilometer data, weather station data, air quality data, radiosonde data, and satellite data. The data were collected at 11 different locations and 2 profiles in northeastern Puerto Rico ([Fig. 1](#); [Table 1](#)), over the years 2008–21, and analyzed jointly to give a summary at urban, montane forest, and rural. Almost all data were collected hourly or subhourly; these were averaged into daily values (if more than 75% of the day's data existed). The exceptions were radiosonde and satellite data,

TABLE 1. Data record information.

Station	Lat (°N)	Lon (°W)	Elev (m)	Land cover	Variables used <sup>a</sup>	Period used	Daily data missing <sup>b</sup>	Data reference
Sabana Field Research Station	18.32	65.73	100	Forest	C, A, P <sup>c</sup>	Feb 2013– May 2021	48%, 71% <sup>c</sup>	C, A: <a href="https://doi.org/10.2737/RDS-2022-0050">https://doi.org/10.2737/RDS-2022-0050</a> ; P: <a href="https://doi.org/10.2737/RDS-2021-0030">https://doi.org/10.2737/RDS-2021-0030</a>
Bisley Experimental Watersheds	18.30	65.75	361	Forest	P, H, T	Jan 2008– Oct 2020	15%	<a href="https://doi.org/10.2737/RDS-2022-0050">https://doi.org/10.2737/RDS-2022-0050</a>
Bisley air quality	18.30	65.75	367	Forest	O	May 2008– May 2021	52%	<a href="https://doi.org/10.2737/RDS-2022-0050">https://doi.org/10.2737/RDS-2022-0050</a>
East Peak Weather Station	18.27	65.76	1012	Forest	W	Oct 2009– May 2021	28%	<a href="https://doi.org/10.2737/RDS-2022-0050">https://doi.org/10.2737/RDS-2022-0050</a>
San Juan ASOS	18.43	66.01	3	Airport	C, W, H, T, P <sup>c</sup>	Jan 2008– May 2021	0.4%, 30% <sup>c</sup>	TJSJ: <a href="http://mesonet.agron.iastate.edu">http://mesonet.agron.iastate.edu</a>
San Juan radiosonde	18.43	65.99	4	Airport	A	Jan 2008– May 2021	61%	RQM00078526: <a href="https://www.ncdc.noaa.gov">https://www.ncdc.noaa.gov</a>
San Juan air quality	18.44	66.05	1	Urban	Ca	Jan 2008– Jan 2021	29%	721270003: <a href="https://www.airnow.gov">https://www.airnow.gov</a>
Bayamón air quality	18.42	66.15	70	Urban	S	Jan 2008– Jan 2021	46%	720210010: <a href="https://www.airnow.gov">https://www.airnow.gov</a>
Cataño air quality	18.44	66.12	5	Urban	O	Jan 2008– Jan 2021	18%	720330008: <a href="https://www.airnow.gov">https://www.airnow.gov</a>
Guaynabo air quality	18.42	66.12	8	Urban	N	May 2015– Feb 2020	74%	720610006: <a href="https://www.airnow.gov">https://www.airnow.gov</a>
Roosevelt Roads ASOS	18.26	65.64	12	Airport	C, W, H, T, P <sup>c</sup>	Sep 2010– Jan 2021	34%, 42% <sup>c</sup>	TJNR: <a href="http://mesonet.agron.iastate.edu">http://mesonet.agron.iastate.edu</a>
Caguas air quality	18.20	66.05	8	Inland	Ca, N <sup>c</sup>	Jan 2017– Jan 2021	80%, 88% <sup>c</sup>	720250007: <a href="https://www.airnow.gov">https://www.airnow.gov</a>
Juncos air quality	18.18	65.92	150	Rural	O, S <sup>c</sup>	Jan 2008– Jan 2021 <sup>d</sup>	28%, 49% <sup>c</sup>	720770001: <a href="https://www.airnow.gov">https://www.airnow.gov</a>
CALIPSO day track	18.1– 18.4	65.9– 66.0	Vary	Various	C, A	Jan 2008– Mar 2021	95% <sup>e</sup>	<a href="http://www-calipso.larc.nasa.gov">http://www-calipso.larc.nasa.gov</a>
CALIPSO night track	18.2– 18.5	66.3– 66.4	Vary	Various	C, A	Jan 2008– Mar 2021	95% <sup>e</sup>	<a href="http://www-calipso.larc.nasa.gov">http://www-calipso.larc.nasa.gov</a>

<sup>a</sup> Key to abbreviations: C = cloud detections, A = aerosol gradients, W = wind speed and direction, H = relative humidity, T = temperature, P = precipitation, O = ozone amounts, S = sulfur dioxide amounts, N = Nitrogen dioxide amounts, and Ca = carbon monoxide amounts.

<sup>b</sup> Average percentage of missing daily data in the entire period January 2013–May 2021.

<sup>c</sup> Variables with this symbol have missing percentages marked with the same symbol.

<sup>d</sup> Sulfur dioxide measurements at Juncos stop in September 2016.

<sup>e</sup> CALIPSO tracks are repeated once every 16 days, so a perfect record would be 15/16 days missing, or 93.8%.

which were collected twice daily (morning and evening) and once every 16 days, respectively.

#### *a. Ceilometer and weather station data at San Juan and Roosevelt Roads airports*

The hourly ASOS data for the airport stations of San Juan and Roosevelt Roads from 2008 to 2021 were accessed from the Iowa Environmental Mesonet (Table 1). This study uses the data of lowest cloud layer base, cloud cover, and weather variables of wind direction, wind speed, precipitation, air temperature, and relative humidity (RH). ASOS instrument details are provided in Nadolski (1998). All ASOS data are summarized to the mean hour or before reporting, unless the weather is changing rapidly, and then shorter time steps are reported. At each station, 3 layers of cloud base heights and cloud cover are automatically calculated from the airport laser ceilometer's 16-s processing intervals. A cloud base height

is the bottom of a vertically continuous layer at a point above the ceilometer at least 100 m thick with no vertical visibility (defined according to a contrast threshold, e.g., 5%). The ASOS network reports cloud cover as “clear” for detection at a fraction 0–0.05, “few” for 0.05–0.25, “scattered” for 0.25–0.5, “broken” for 0.5–0.87, and “overcast” for 0.87–1. For calculation of cloud cover in this study, the five cover categories were converted to cloud cover fraction using the middle of the range or 0 for “clear,” 0.1875 for “few,” 0.4375 for “scattered,” 0.75 for “broken,” and 1 for “overcast.” The weather variables were used by this study as ASOS-reported values, except for wind-direction data, which were summarized from degrees to wind rose octants.

The averaging of the ASOS data into daily values is straightforward, except for cloud heights and wind direction. For cloud heights, no-detections are ignored in the averaging since the ASOS algorithm already smooths the data. Only

layer-1 heights are used in the statistical analysis in this study. Layer-1 heights are only averaged with other layer-1 heights, across time, for daily values of cloud lowest mean height. For wind direction, the fraction of the day the wind is in each wind rose octant is multiplied by the wind speed to give an average wind strength in each octant. All wind octants were analyzed in this study, but only two octants, northeast ( $45^{\circ}$ – $90^{\circ}$ ) and southeast ( $90^{\circ}$ – $135^{\circ}$ ) are included in the results, because the wind very rarely comes from other directions in northeastern Puerto Rico.

*b. Ceilometer, weather station, and ozone data in the Luquillo Experimental Forest*

A Vaisala CL31 laser ceilometer was installed at 100-m elevation 7 km northeast of the northwest-trending ridge-line that connects two of the higher peaks of the Luquillo Mountains in the LEF (Table 1). This study uses data from February 2013 through April 2021 to compute lowest cloud layer base, cloud cover (or sky frequency), daytime MLH and MLH frequency (temporally frequency during the day that a distinct MLH is detected). The laser uses lidar technology, shooting short pulses of light vertically and measuring the time and strength of light return at the receiver that is backscattered by the aerosols, or the backscatter profile. The presence of a cloud layer is identified by a strong return, and then time gives a height of the cloud base. Below the cloud layer, the mixed layer of the atmosphere has a higher aerosol concentration than the air above it, so a sharp negative gradient (a minimum) in the backscatter profile indicates an aerosol layer boundary (associated with a time that gives the height of the boundary). The ceilometer processes data at 16-s intervals, like the ASOS ceilometers, and reports three layers of cloud base heights up to 7620 m above the instrument (25 000 ft) and three layers of aerosol heights up to 4000 m (13 123 ft) above the instrument, from 770 backscatter profiles. Since the instrument is at 100-m elevation, this translates to an altitude of 7720 and 4100 m. Aerosol gradients are not computed when it is raining (Vaisala Oyj 2010).

The LEF ceilometer data, cloud base layers and the aerosol layers, were then further processed to mimic the ASOS algorithm for designating hourly layers so that the atmospheric conditions could be compared regionwide. First and foremost, the ASOS cloud algorithm is intended to provide guidance to aircraft in real time and not produce a scientific record, so algorithm description is not explicit, and some reporting decisions are not quantifiable. However, the general method of the ASOS algorithm is effective at summarizing the overall low cloud system by smoothing data from a noisy instrument with *k*-means clustering (Hartigan and Wong 1979).

The lowest aerosol gradient minima above the surface inversion layer can be considered a representative of the MLH even in an area with complex terrain (Mues et al. 2017; Ketterer et al. 2014). In this study, this is layer 2; layer 1 is identified as the surface inversion layer. Only daytime values are analyzed, as these were shown to have a more distinct layer 1 and 2 to justify use of the method. Some

concerns with this method have been that composite hourly averages may be averaging across layers since layers may be discontinuous in time and the highest layer may present as the lowest layer at a time if all other layers are not detected at that time (Haefelin et al. 2012). However, a solution is to use clustering to detect the aerosol levels and thereby reduce the variation in layer designation (Liu et al. 2019). To this end, the aerosol gradient minima values as reported by the ceilometer were processed into hourly layers with the clustering ASOS algorithm along with the cloud base values.

The intent of the ASOS algorithm as described by Nadolski (1998) was reproduced here to the best extent possible. First, every two 16-s data points were averaged to produce three layers of cloud base and three layers of aerosol boundaries, with nondetections ignored unless both points are nondetections. Then, every 64 s, the most recent 60 two-point averages were processed together (32 min of data) to give a smoothed value of the layer heights and sky cover recorded every 64 s. The following procedure was followed separately for clouds and aerosols.

- 1) The fraction of the 60 points of time with at least one layer detected for clouds and two layers detected for aerosols is saved as sky-cover fraction.
- 2) Bins are made from 240 heights. The 60 points of time with the last 20 points of time used twice (so 80 points of three layer heights or no-detections each) are included. The last 20 points are double weighted to be more responsive to the latest changes in sky condition. The heights are converted from meters to feet ( $1\text{ m} \approx 3.3\text{ ft}$ ) and then binned to the nearest 100 ft between 0 and 5000 ft, to the nearest 200 ft between 5000 and 10000 ft, and to the nearest 500 ft for heights above 10000 ft.
- 3) The bins are clustered into five layers (if more than five were detected). This was done using *k*-means clustering. The number of hits in each layer is noted. After clustering, each layer height is rounded to the nearest 100 ft between 0 and 5000 ft, to the nearest 500 ft for between 5000 and 10000 ft, and to the nearest 1000 ft for heights above 10000 ft; this possibly combines some layers.
- 4) Up to three of the layers are selected as ASOS “priority and meteorologically significant” and recorded. This study interpreted this to mean “select the three layers with the most hits that were hit more than 5% of the time” (for an ASOS “few” cover classification, this is 5 of 80 possible hits). If there are ties, the lowest heights were selected.

Last, for hourly reporting, all the identified layers of the 64 s periods in an hour (56–57 periods) were averaged for three layer heights (with no-detections ignored unless all points are no-detection) and a sky-cover fraction. Layer-1 heights are only averaged with other layer-1 heights for daily values of cloud lowest mean height. Layer-2 heights are only averaged with other layer-2 heights, but only during the daytime hours (0700–1900 LT) for aerosol gradient minima estimates of the MLH. The sky-cover fractions were put into one of the five ASOS cover categories as discussed previously. Figure 2 shows

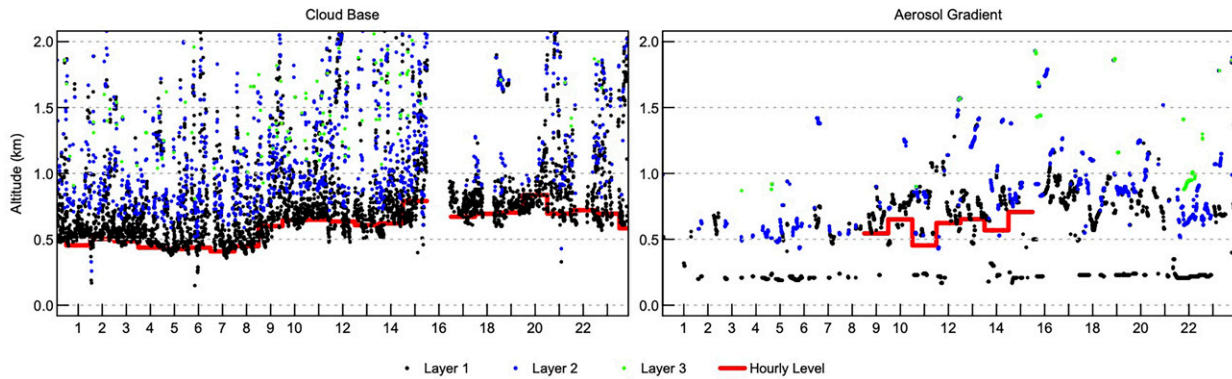


FIG. 2. Unprocessed and processed data hourly (0–24) from the ceilometer (detecting clouds up to 7620 m and aerosols up to 4000 m from the ground) from an example day, 29 Jun 2013. The lowest hourly level as processed in the ASOS method is shown in red. No red line means either a nondetection hour from missing data or high data, or an hour with rain or not during daylight hours in the case of the aerosol gradient (and thus no MLH is estimated).

an example of this ASOS algorithm in practice on a random day (and representative of a typical day), with ceilometer layer data as points and the computed ASOS algorithm hourly lowest cloud base or MLH as a red line. These red line values were averaged for the daily values.

Hourly precipitation, RH, temperature, wind speed, and wind direction data have been collected over the years at several weather stations around the LEF for differing periods of record (Van Beusekom et al. 2017). This study used the precipitation, relative humidity, and temperature from the station with the most complete and longest period of record located within the Bisley Experimental Watersheds at 361 m MSL (Table 1). The wind direction was taken from the forest station at the highest elevation available, East Peak Weather Station at 1012 m, as this station is more indicative of the general wind direction hitting the LEF and not subject to the complicated topographic and vegetative wind-shading effects lower down on the mountain.

Last, ozone concentration data were collected in the LEF for an air quality record at the Bisley location. These data were collected since 2008 as an hourly average, using a 2B Technologies Ozone Monitor model 202. The instrument measures ozone concentration through UV absorption.

All forest data were averaged to daily values as with the ASOS data. The MLH no-detections were ignored in the averaging just as the cloud no-detections were ignored. Wind strength in each octant was collected by the hour here, so averaging to daily average wind strength in each octant is straightforward. The ceilometer cannot detect the MLH when it is raining, so the daily daytime fraction of MLH detection only uses the daytime MLH measurements when the weather station at Sabana Field Research Station (collocated with the ceilometer) records no precipitation. This station is missing large amounts of precipitation data, so the MLH frequency is also missing a large amount of the record.

#### c. Radiosonde data at San Juan

Radiosonde profiles were available for 2008–21 at San Juan only two times daily, 0700 and 1900 locally, from the

Integrated Global Radiosonde Archive (Durre et al. 2009). The archive radiosonde profiles were used to calculate the MLH at 0700 and 1900 LT at level of the minimum vertical gradient of refractivity, a method that has been found to work well in the tropics (Basha and Ratnam 2009). In this study, it was found that this method was not as influenced by surface inversions as other methods such as the parcel method or the maximum vertical gradient of potential temperature. For global comparison of methods, see Seidel et al. (2010). The daily mean of these radiosonde MLH values was compared with the daily mean of the 0700 and 1900 LT hours of the MLH computed from the ceilometer at the LEF. These are not ideal times for MLH calculation because of the proximity to the night hours and the possibility of stronger surface inversions, but these are the only data on the island to compare with the LEF MLH data.

#### d. Air quality data at city and rural locations

The U.S. Environmental Protection Agency (EPA) collects and records air quality at several locations across Puerto Rico as part of the Clean Air Act [Title 42, U.S. Code 7401–7671q (1970); <https://www.epa.gov/clean-air-act-overview/clean-air-act-text>]. This study used the hourly ozone concentration data at Cataño and Juncos (Fig. 1) to compare with the ozone concentration data collected in the LEF. The Cataño station is in the greater San Juan metropolitan area, close to the other San Juan weather and atmospheric measurements. The Juncos station is located inland from the coast 10 km, and over 15 km from the location of the Roosevelt Roads weather and atmospheric measurements. However, the station is rural and on the eastern side of the island. It is the closest station to the rural Roosevelt Roads area.

The EPA also collects hourly concentrations of nitrogen dioxide (NO<sub>2</sub>), sulfur dioxide (SO<sub>2</sub>), and carbon monoxide (CO), which come from combustion processes (e.g., gasoline and diesel). The EPA data were used here in areas around San Juan (Guaynabo, Bayamón, and San Juan stations for NO<sub>2</sub>, SO<sub>2</sub>, and CO, respectively) and the area away from the main city (Caguas, Caguas, and Juncos for NO<sub>2</sub>, SO<sub>2</sub>, and

CO, respectively) to compare with the MLH measurements and use as anthropogenic pollution metrics.

#### e. Satellite data

*Cloud–Aerosol Lidar and Infrared Pathfinder Satellite Observation (CALIPSO)* satellite vertical feature mask data (Winker et al. 2009) 2008–21 were analyzed for information on aerosol types in the region to compare from 2008 to 2021. There are two tracks in the region considered (Fig. 1); the northwest/southeast trending track is the daytime orbit, and the opposite direction the nighttime orbit (geographically located to the west in this study). Tracks are repeated at a 16-day interval and each satellite overpass records vertical profiles of aerosol type detected in 300-m horizontal by 30-m vertical cells up to 8200 m in altitude (data extend up to 30 km, but those data are not discussed here). This study only uses the data up to 4100 m (137 cells per profile), as that is the highest altitude the LEF ceilometer detects aerosol layers. Each day CALIPSO measured on a track (the two tracks were analyzed separately), the four closest profiles to the LEF were used as that day's data. In each profile, the spatial frequency of each aerosol type was calculated, and then the average frequency from the four profiles was recorded as the daily value. This geographic spatial extent is shown in Fig. 1; each track is approximately 17 km long and is not across urban areas or the montane forest. Aerosol detection is more sensitive in nighttime profiles than in daytime profiles (Liu et al. 2009).

Aerosol type is reported by CALIPSO from criteria placed on the values of extinction-to-backscatter ratios in the integrated (from layer base to layer top) lidar backscatter profiles (Omar et al. 2009). These criteria were based on research of the CALIPSO group on a 9-yr global aerosol dataset. The types identified are clean continental, clean marine, dust, polluted continental, polluted dust, and smoke. A cell must be identified as an aerosol cell to be given a type (and not a cloud, land/ocean, or clear air). In this study, the types were further combined into clean (clean continental and clean marine, pollution (polluted continental and smoke), and dust (dust and polluted dust).

#### f. Analysis of data including statistics

Data were summarized to three general locations: city (near San Juan), montane forest (LEF), and rural (Roosevelt Roads and Juncos). The data at all three sites suffer from data quantity and quality issues. Data collection in the forest is difficult due to tropical storms and remoteness. New and repaired instruments may cause magnitude jumps in data, for example, the documented effects of improvement in radiosonde machinery (Miller et al. 2018). As for ASOS sites, their function is to assist aviation in real time, so data are not corrected beyond immediate processing. Also, the magnitude of data will not be representative of the whole location since linear gradients in climate data exist along the northeast Puerto Rico elevational gradient (Van Beusekom et al. 2015; Waide et al. 2013). Because of these issues, trends and anomalies in the data time series are not easily interpretable. In this study,

the annual pattern of the data and the time series of correlations between data types are studied to minimize the effects of these issues. Infrequent magnitude shifts over the years of data and linear magnitude differences in site choice will minimally affect the monthly correlation. They will affect the magnitude of the annual summaries, but the pattern of the average annual values will be minimally affected.

Daily data of each type at each location were first plotted over the period of record for an annual pattern by month, using violin plots. Violin plots are a kernel density plot with box plot, such that bimodal and skew behavior is identified in the data. Outliers were removed when values fell outside the values of 1.5 times interquartile range. Monthly median time series were computed and plotted to look for major changes across the environmental events and to visually show the record of measured monthly data, keeping in mind the above data quality issues. Only months with at least 15 measurement days were plotted.

Last, monthly correlations of the daily data were computed to look for changes in the near-surface atmospheric behavior across the period of record and across environmental events. A least 15 measurement days in a month were required to compute correlation. Correlation computed on each month of data separately will be minimally affected by infrequent magnitude shifts in data from instrument changes (generally a month with an instrument change resulted in missing data before the change, meaning at most one month's calculations were affected but likely the data were just missing for the month). Atmospheric variables were correlated with each other, and then weather variables were correlated with each other, and then atmospheric variables were correlated with weather variables. Satellite data were not included in the correlations as these data were only collected every 16 days. All correlations between variables were computed as Pearson product-moment correlations measuring linear correlation;  $p < 0.05$  was considered significant. Data was prewhitened to remove autocorrelation, trends, and seasonal patterns before correlation (Casella and Berger 2001). This meant that the resulting correlations are not a reflection of seasonal weather pattern agreement, but that the white noise in one variable must correlate with the white noise in the other variable for the variables to be considered "correlated."

## 4. Results

Of the three kinds of plots described in the previous section, the data plotted by month (Figs. 3 and 4) showed the clearest results, with distinct annual patterns in every atmospheric at every location; the seasonality of the San Juan area often looking like an average of the seasonality of the LEF and Roosevelt Roads areas. The data plotted as monthly median time series (Figs. 5 and 6) showed that environmental changes largely did not change the annual patterns. The correlation between the data (Figs. 7 and 8) supported the result that the effect of the seasonal weather patterns was much stronger than the effects of the specific environmental events, with the correlations showing expected patterns of weather

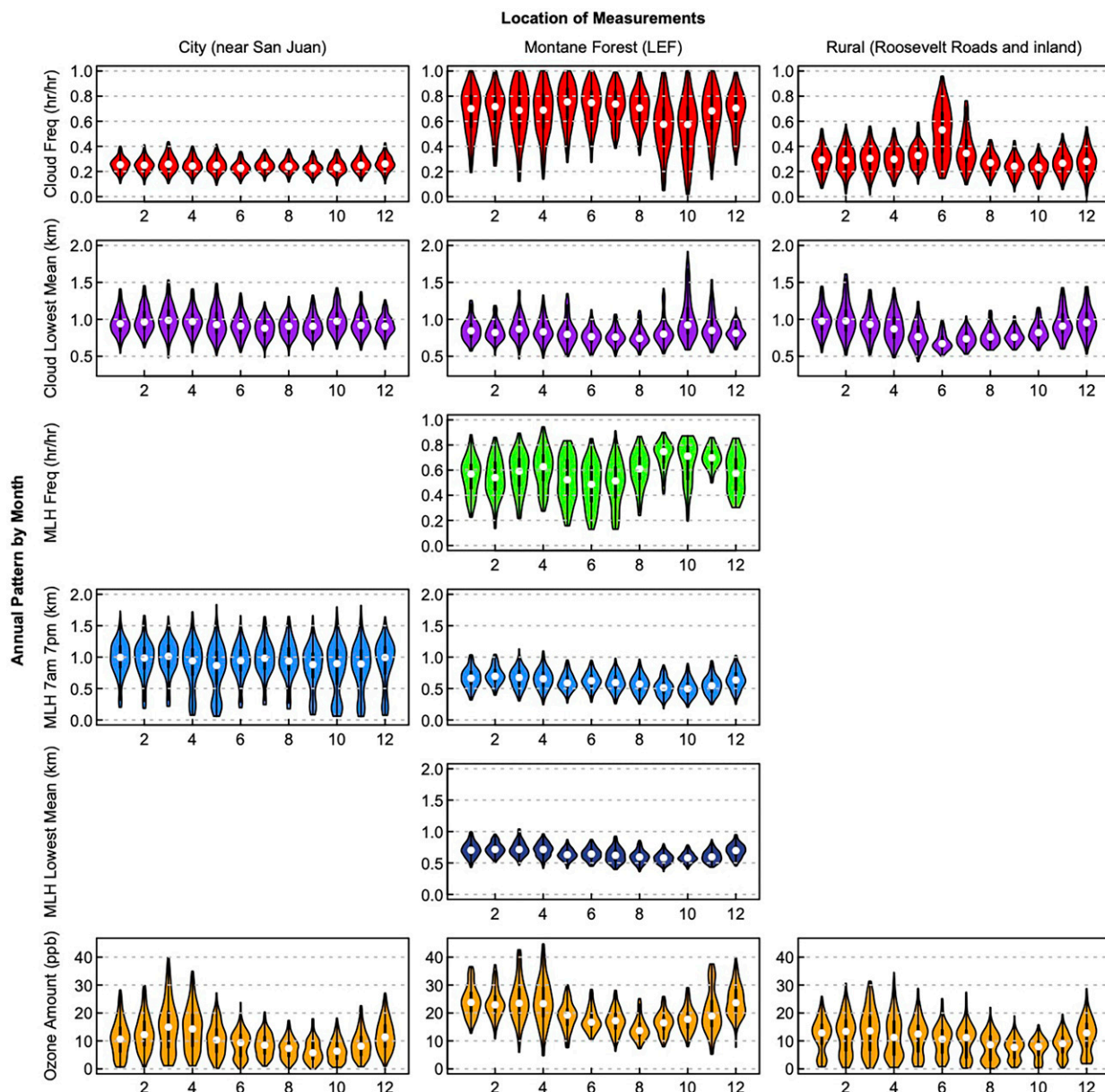


FIG. 3. Monthly (1–12 = Jan–Dec, respectively) violin plots of all daily average atmospheric variable altitudes, frequencies, and concentrations. The medians are marked with a white dot, and outliers are excluded. Frequency is a temporal frequency of hours with a cloud or aerosol detected in them, from 24 h in a day (detecting clouds up to 7620 m and aerosols up to 4000 m from the ground).

physics, across-site differences in strengths of correlation, and only a few short-lived changes with environmental events. Specific results follow. To focus the results on the new information learned from this study, the annual pattern and monthly median time series of the weather variables are included in the online supplemental material only (see supplemental Figs. S1 and S2).

#### a. Annual patterns

For the atmospheric variables, the largest geographical difference in was seen in the cloud frequency (Fig. 3). The cloud

frequency was much higher on the mountain, as expected from orographic effects (red in Fig. 3). The cloud frequency in San Juan was almost seasonally consistent. The low cloud height was remarkably homogenous spatially and temporally across the region, with the most seasonality seen at Roosevelt Roads (purple in Fig. 3). This phenomenon of consistent low clouds was discussed in previous research and hypothesized to contribute to the persistence of the cloud forest in the LEF (Van Beusekom et al. 2017).

In contrast, the MLH, ozone concentration, and air quality data showed relative geographical agreement in annual

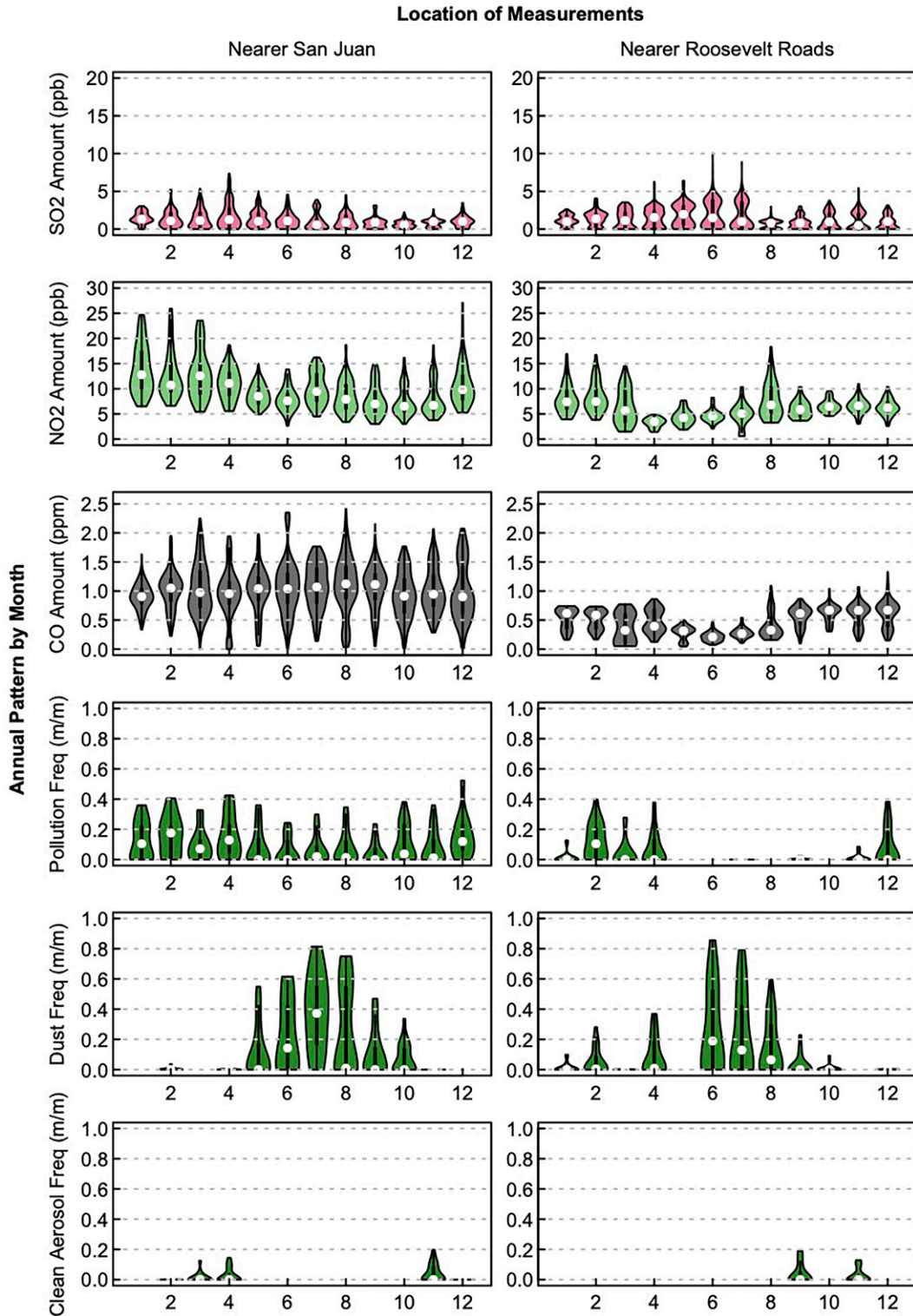


FIG. 4. Monthly (1–12 = Jan–Dec, respectively) violin plots of all daily average pollution concentrations and aerosol type *CALIPSO* frequencies. *CALIPSO* data are from vertical profiles 0–7720 m in altitude for clouds and 0–4100 m in altitude for aerosols at four locations every 2 weeks on each of the night (nearer San Juan) and day (nearer Roosevelt Roads) tracks. The medians are marked with a white dot, and outliers are excluded. Frequency is a spatial frequency of vertical cells with a cloud or aerosol detected in them, from the ground to the altitude of 4100 m.

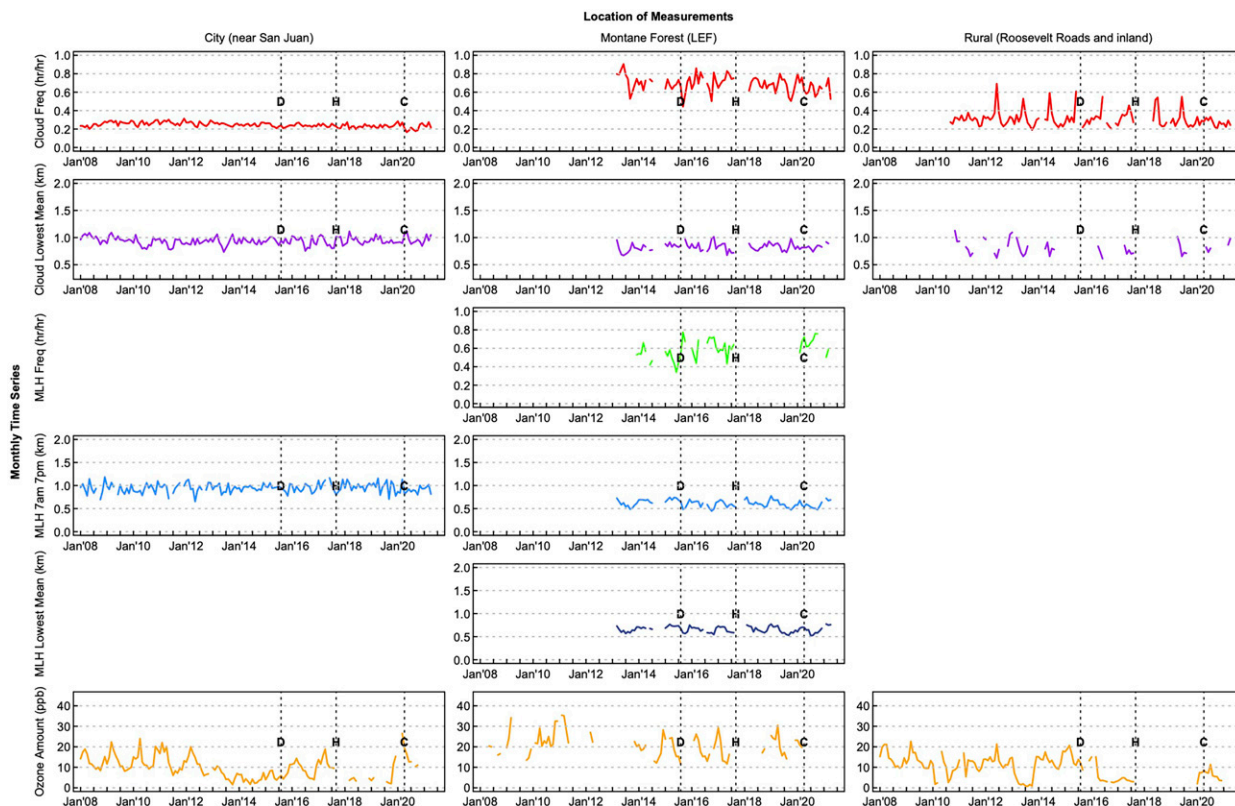


FIG. 5. Monthly median time series of daily average atmospheric variable altitudes, frequencies, and concentrations. Months with less than 15 days of data are not given a value; “D” marks the middle of the islandwide drought, “H” marks Hurricanes Irma and María, and “C” marks the start of the COVID-19 island lockdowns. Frequency is a temporal frequency of hours with a cloud or aerosol detected in them, from 24 h in a day (detecting clouds up to 7620 m and aerosols up to 4000 m from the ground).

patterns. The mixing layer height measured at the LEF by the ceilometer and at San Juan by radiosonde both showed a slight rise in the median values in the winter (light blue, Fig. 3). Overall magnitude of MLH computed from radiosonde measurements vary by 1000 m globally depending on the calculation method (Seidel et al. 2010); here it was found that the patterns of the measurements were very similar across methods, but the median magnitude varied by several hundred meters. Thus, the magnitude differences between the MLH at San Juan and the LEF should not be directly compared. The ozone concentration (orange in Fig. 3) across the region had the highest amounts (but still low, or moderate, in terms of air quality) in the winter. Winter ozone concentration peaks are attributed to the seasonal low in moisture (precipitation and humidity), versus temperature control, which would result in a summer peak (Jury 2017). The LEF has higher ozone concentrations, as expected due to higher elevation (Clifton et al. 2014).

The annual patterns of air quality data and satellite measurements of aerosol type (Fig. 4) show quite a bit of similarity across the region, considering the sparsity of the air quality data and the 16-day track repeat of the satellites, as well as the night and day satellite differences. These patterns suggest which types of aerosols might have been part of the land–atmosphere interaction at different times of the year. Winter had higher

nitrogen dioxide concentration, as well as more pollution throughout the air column (rows 2 and 4 in Fig. 4), both somewhat like the annual pattern seen in ozone concentration at all sites (orange in Fig. 3). Dust dominated in the summer months (row 5 in Fig. 4).

#### b. Monthly time series

The key finding in the monthly time series is that no clear changes in the atmospheric data were seen after the 2015 drought, Hurricanes Irma and María. However, with the COVID-19 island lockdowns, Roosevelt Road cloud frequency data did not exhibit the usual summer spike in cloud frequency (red line at summer 2021 in Fig. 5), there is a decrease in cloud frequency at San Juan, and there is a high observance frequency of the MLH at the LEF.

In the air quality and satellite data (Fig. 6), again, only the event of the COVID-19 island lockdowns showed any changes. The carbon monoxide amounts increased right as the lockdowns began in both locations (gray in Fig. 6). All other EPA sites in northeastern Puerto Rico recorded this same spike (data not shown). At San Juan, the carbon monoxide concentration decreased after the spike to a lower level than baseline 3 months later. This persisted until at least January 2021 (when the current data record stopped).

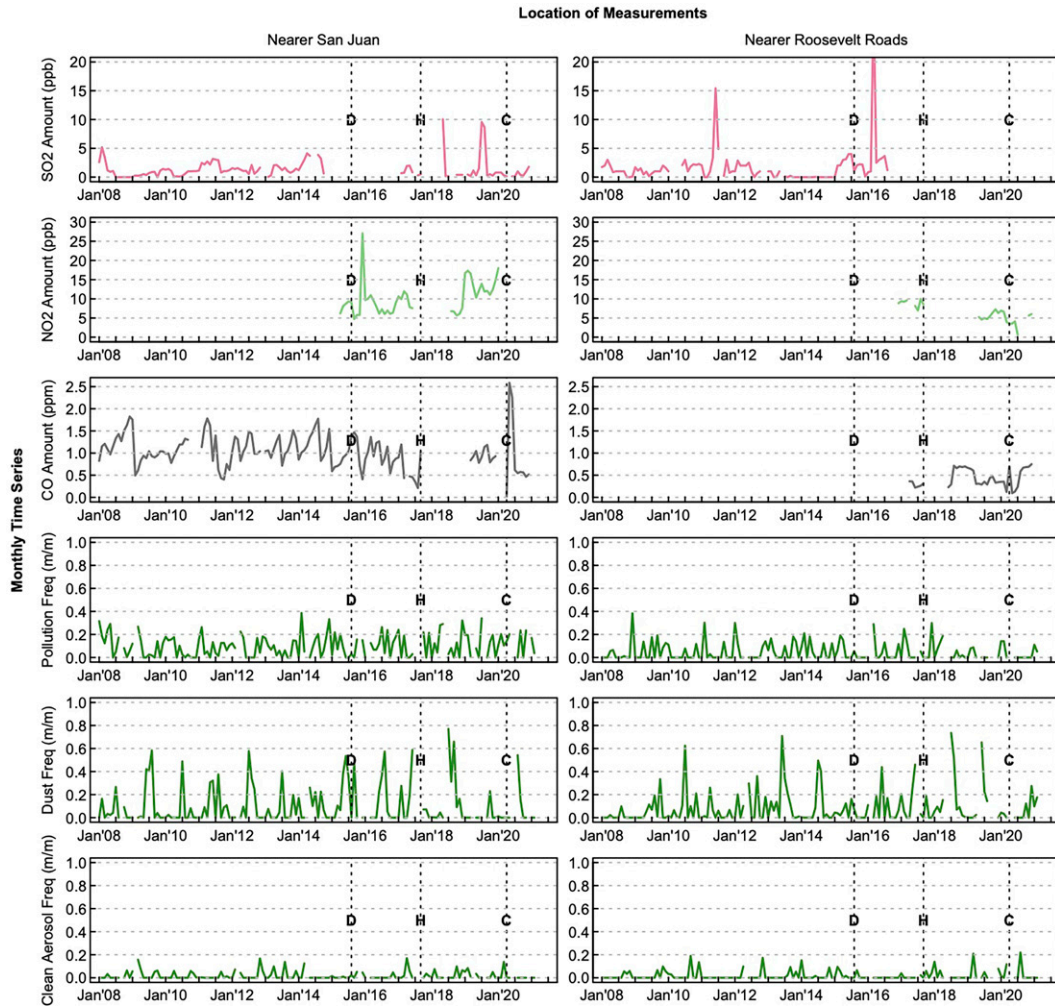


FIG. 6. Monthly median time series of daily average pollution concentrations and aerosol type *CALIPSO* frequencies. *CALIPSO* data are from vertical profiles 0–4100 m in altitude for aerosols at four locations every 2 weeks on each of the night (nearer San Juan) and day (nearer Roosevelt Roads) tracks. Here, “D” marks the middle of the islandwide drought, “H” marks Hurricanes Irma and María, and “C” marks the start of the COVID-19 island lockdowns. Frequency is a spatial frequency of vertical cells with a cloud or aerosol detected in them, up to the altitude of 4100 m.

So, overall, a lower amount of carbon monoxide would have been recorded in San Juan during lockdown agreeing with assertions on cities worldwide (Venter et al. 2020); but to be precise, this was a large increase followed by a decrease.

c. Correlation time series

Figures 7 and 8 highlight the usual correlation patterns found between the variables that show geographical differences and changes in response to environmental events, more apparent here than in the time series plots of Fig. 5 and 6. The first of these figures (Fig. 7) is correlation of variables with the same kinds of variables (i.e., ozone concentration with atmospheric variables and wind with weather variables), that showed unexpected relationships. The second figure (Fig. 8) shows the correlation of atmospheric variables with weather variables.

Geographical differences were seen in several of the atmospheric variable correlations. Ozone amounts (row 1 in Fig. 7) often correlated positively with cloud frequency (red), but only at San Juan, and instead at the LEF ozone amounts correlated more often positively with MLH (blue). Nitrogen oxide amounts (green) correlated well with ozone amounts when data were available (row 1 in Fig. 7) at San Juan as expected in a higher nitrogen oxide environment; there is no correlation inland during times of data overlap (only 2019–21; see Figs. 5 and 6 for data period of record). Cloud base height (purple) negatively correlated with carbon monoxide amounts at San Juan (row 2 in Fig. 7), in agreement with pollution acting as cloud condensation nuclei. Notably, the lower carbon monoxide concentration in San Juan during COVID-19 lockdowns only correlates with higher cloud bases in December

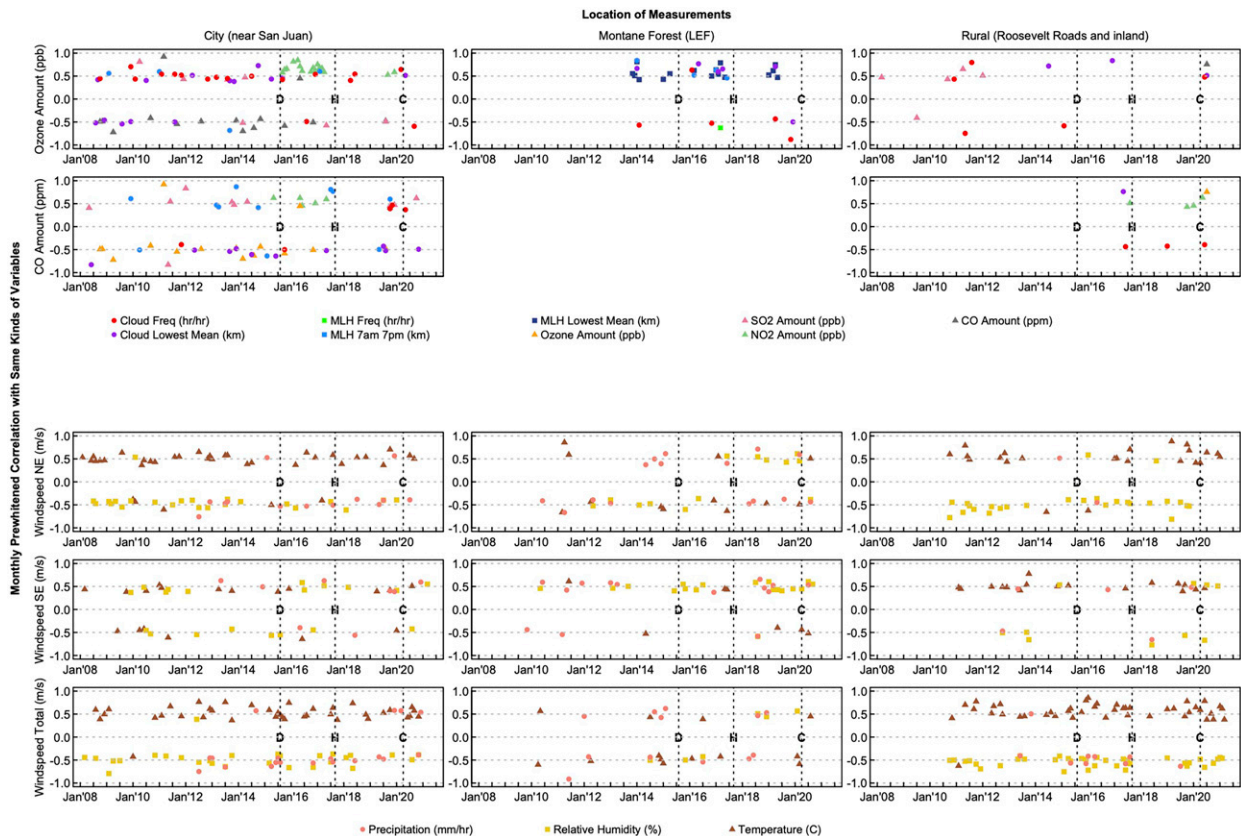


FIG. 7. Monthly correlation of daily average atmospheric and weather variables with themselves at each location, for unexpected variable relationships only. (This is ozone and carbon monoxide with other atmospheric variables, and wind with other weather variables.) Only correlations that are significant at the  $p < 0.05$  level, with more than 15 days of data per month for the calculation, are shown; “D” marks the middle of the islandwide drought, “H” marks Hurricanes Irma and María, and “C” marks the start of the COVID-19 island lockdowns.

2020 after 6 months of lower carbon monoxide pollution (June 2020 to December 2020; gray in Fig. 6).

In the weather variable correlations, the dominance of wind in the Caribbean trade wind system is show; but again, there were geographical differences in the general pattern and with the environmental changes. RH correlated negatively and temperature correlated positively often with the total wind speed and the dominant direction wind speed (northeast direction, the trade winds), but only at San Juan and Roosevelt Roads and not at the montane forest of the LEF (rows 3 and 5 in Fig. 7). At the LEF, the cloud formation precursor of RH correlated positively with the less-dominant direction wind speed (southeast direction) much more frequently after the defoliation events of the 2015 drought and Hurricanes Irma and María (row 4 in Fig. 7), suggesting the southeast wind speed and increases in humidity were more closely related during losses of greenness.

When the atmospheric variables were correlated with the weather variables, the direction (positive or negative) of the correlations were similar across locations; but the strength, the number of months with significant correlation, and the effects of the environmental events varied between sites (Fig. 8). Cloud

frequency (red) and cloud base height (purple) correlated with weather variables oppositely as expected, but cloud base height correlated much more often than frequency at San Juan, and the opposite was true at the LEF and Roosevelt Roads. To some extent, the cloud frequency correlation (red) with the weather variables at San Juan and the LEF got stronger and stronger after each event, the 2015 drought, Hurricanes María and Irma, and the COVID-19 island lockdowns; all events that reduced land signatures (loss of greenness or loss of land pollution). The correlation between RH and cloud frequency (red row 5 in Fig. 8) supports this notion the most out of all the variables.

Ozone amounts correlated positively with dominant direction wind speed (northeast, the trade winds) and total wind speed (orange rows 1 and 3 in Fig. 8). When comparing the correlated months with the ozone period of record (orange in Fig. 5), it is noticeable that there is positive correlation with ozone concentration and total wind speed at San Juan and Roosevelt Roads when there are data but not at the LEF. The ozone concentration at the LEF correlates positively with the northeast direction wind speed only, and only around the time of the 2015 drought (orange row

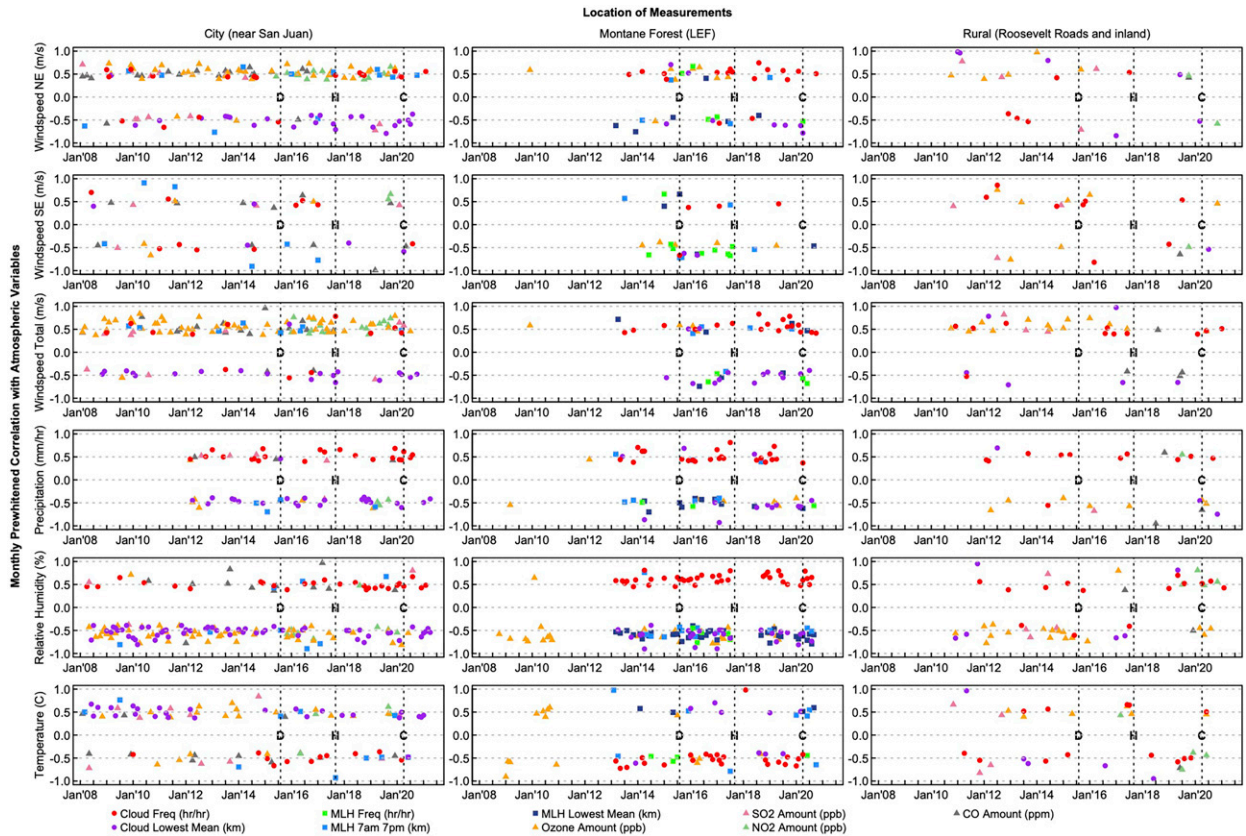


FIG. 8. Monthly correlation between daily average weather variables and daily average atmospheric variables at each location. Only correlations that are significant at the  $p < 0.05$  level, with more than 15 days of data per month for the calculation, are shown; “D” marks the middle of the islandwide drought, “H” marks Hurricanes Irma and María, and “C” marks the start of the COVID-19 island lockdowns.

1 in Fig. 8). The strongest relationship was with humidity, negative in all locations, which agrees with previous research in lower pollution regions (Dawson et al. 2007; Camalier et al. 2007).

The exception to the general pattern of correlation directional (positive or negative) agreement across sites was the MLH and anthropogenic pollution sources. The mixing layer height correlated positively with the less-dominant direction wind speed (southeast) at the LEF and negatively with the dominant direction wind speed (northeast, the trade winds), and the opposite pattern (negative to no correlation) was seen at San Juan (blue rows 1–3 in Fig. 8). The anthropogenic pollution sources of nitrogen oxide and carbon monoxide correlated well (positively) with wind speed at San Juan only, but not inland (light-green and gray triangles in row 1–3 in Fig. 8), even though ozone correlation was strong (orange). The nitrogen oxide (light-green triangles) inland did not have a lot of data, but whenever it did it presented correlations different to those at San Juan; see positive correlation with RH and negative correlation with temperature 2019–21 inland (rows 5 and 6 in Fig. 8). The nitrogen oxide concentration correlation patterns suggest the northeast area away from San Juan has a critically low enough level of anthropogenic pollution influence in comparison

with San Juan such that the ozone is not being driven by the reaction with nitrogen oxide there.

### 5. Discussion

Although much has been made of the potential for environmental changes to alter near-surface atmospheric behavior, the results here show seasonality driven by strong easterly ( $80^{\circ}$ – $90^{\circ}$ ) trade winds transmitting regional oceanic patterns over terrain dominate the system in northeastern Puerto Rico. Events that reduce the land signature, (reducing greenness: e.g., drought and hurricanes, or reducing land pollution: e.g., COVID-19 lockdown) perhaps only strengthen the transmission of the oceanic pattern. In evidence of the domination of the trade winds on the system, increasing cloud frequency and decreasing base height, increasing mixing layer height, increasing ozone and pollution concentration all correlated well with increasing wind strength from the east. Clouds were consistently low from the coast inland. Cloud frequency correlated more with humidity the more the land signature was lost in events. Ozone amounts were strongly negatively correlated with humidity even in the metropolitan area, patterns that agree with low pollution from oceanic air influence.

The second dominating factor after the trade winds was the mountainous terrain. The orographic effect at the mountains collected clouds and precipitation at the LEF. There was more humidity at the LEF during stronger southeast winds, which are weaker than the dominant northeast winds. This agrees with data-driven modeling in Puerto Rico that shows weaker winds having a convergence zone on island and assisting orographic lift, but stronger winds having a convergence zone off island (Jury 2020). Furthermore, theoretical models of low barrier mountains (e.g., the height of the mountains in Puerto Rico) show more orographic moisture with winds under  $10 \text{ m s}^{-1}$  increase, but no increase in moisture when winds get stronger (Colle 2004). The orographic effect may have been stronger after losses in greenness, agreeing with the theory put forth by Miller et al. (2019) that reducing surface roughness (i.e., via trees) could make the orography more efficient.

With climate change, some modeling studies have trade winds strengthening and shifting more southeast to reduce orographic lift at the Luquillo Mountains (Comarazamy and González 2011; Hall et al. 2013). But newer studies point to increasing streamflow trends from the western side of the island (while holding steady on the eastern side) and suggest trade winds may be weakening, thus strengthening orographic lift and consequently projecting more moisture islandwide (Jury 2020). Newer evidence also shows Saharan dust decreasing in the future (Evan et al. 2016). If the trade winds weaken and southeast wind is more prominent, results in the study support orographic moisture increasing and the MLH at the LEF rising. Consequently, ozone concentration in the LEF may increase, and without the trade winds low clouds may become less annually consistent in the LEF and associated cloud forest. Away from the mountains in San Juan, if the trade winds weaken, results in the study support the MLH lowering; this is in line with theories of general MLH behavior and the influence of Saharan dust in the Caribbean (Jury and Santiago 2010). A lower MLH at San Juan could concentrate air pollution, however, higher rainfall wash with decreasing Saharan dust could counteract any air pollution increases.

Climate change does increase potential for environmental events. There might be more frequent large losses of greenness in the future, as hurricanes are projected to be more intense (Yoshida et al. 2017) and droughts will be a persistent feature of Caribbean climate, whether their frequency increases or not (Karmalkar et al. 2013). Losses of greenness may make orographic effects stronger as discussed above, but at some level of frequency of disruption, loss of transpiration (contributing 50% of the moisture; Jury 2020) may raise cloud base. Global emissions of pollution are increasing, yet cleaner energy sources could help offset this. The carbon monoxide pollution changes during the COVID-19 lockdown (sharp increase followed by a more persistent decrease) did correlate with a higher cloud base, but only after 6 months of lower carbon monoxide, so near-surface atmospheric changes with pollution changes would be expected to be gradual. However, the public health effect of any increase in pollution can be significant (Subramanian et al. 2018).

## 6. Conclusions

This study examined the near-surface atmospheric behavior in the tropics by using a large array of observational data types in different locations in northeastern Puerto Rico over 13.5 years. Northeast Puerto Rico is typical of the wet extreme of high islands of the Caribbean, with strong trade winds, complex terrain, and frequent environmental disturbances. With current conditions, near-surface atmospheric behavior is driven by the interplay of the trade winds and the terrain. So, variation in near-surface atmospheric behavior is seasonal and geographical, with the most variation seen in the mountainous areas that are influenced by both factors. The results here show the disturbances do impose variation on the near-surface atmospheric behavior, but these influences are relatively short-lived. It may be possible that in the future an increase in intensity or rate of disturbance could surpass a critical amount, resulting in more persistent change in the near-surface atmospheric behavior through land-atmospheric interaction. With more certainty, this study suggests any climate change effects on the trade winds will be an integral component of the future land-atmosphere interaction in the Caribbean.

*Acknowledgments.* The authors thank Carlos Estrada, Samuel Moya, María M. Rivera, Humberto Robles, and Carlos Torrens for assisting with field data and Ariel E. Lugo and Ferdinand Quiñones for comments on an earlier version of the paper. Additional support was provided by the Luquillo Critical Zone Observatory (National Science Foundation Grant EAR-1331841) and the Luquillo Long-Term Ecological Research Site (National Science Foundation Grant DEB-1239764). All research at the International Institute of Tropical Forestry is done in collaboration with the University of Puerto Rico. Any use of trade, product, or firms' names is for descriptive purposes only and does not imply endorsement by the U.S. government.

*Data availability statement.* All data collected by the authors are hosted on the USDA Forest Service Research Data Archive (<https://www.fs.usda.gov/rds/archive/Catalog>). The specific DOIs for the data are listed in Table 1 and are given in González et al. (2022, 2021).

## REFERENCES

- Barbaro, E., J. V.-G. de Arellano, H. G. Ouwersloot, J. S. Schröter, D. P. Donovan, and M. C. Krol, 2014: Aerosols in the convective boundary layer: Shortwave radiation effects on the coupled land-atmosphere system. *J. Geophys. Res.*, **119**, 5845–5863, <https://doi.org/10.1002/2013JD021237>.
- Basha, G., and M. V. Ratnam, 2009: Identification of atmospheric boundary layer height over a tropical station using high-resolution radiosonde refractivity profiles: Comparison with GPS radio occultation measurements. *J. Geophys. Res.*, **114**, D16101, <https://doi.org/10.1029/2008JD011692>.
- Brown, S., and A. E. Lugo, 2017: Trailblazing the carbon cycle of tropical forests from Puerto Rico. *Forests*, **8**, 101, <https://doi.org/10.3390/f8040101>.

- Camalier, L., W. Cox, and P. Dolwick, 2007: The effects of meteorology on ozone in urban areas and their use in assessing ozone trends. *Atmos. Environ.*, **41**, 7127–7137, <https://doi.org/10.1016/j.atmosenv.2007.04.061>.
- Casella, G., and R. L. Berger, 2001: *Statistical Inference*. 2nd ed. Cengage Learning, 660 pp.
- Clifton, O. E., A. M. Fiore, G. Correa, L. W. Horowitz, and V. Naik, 2014: Twenty-first century reversal of the surface ozone seasonal cycle over the northeastern United States. *Geophys. Res. Lett.*, **41**, 7343–7350, <https://doi.org/10.1002/2014GL061378>.
- Colle, B. A., 2004: Sensitivity of orographic precipitation to changing ambient conditions and terrain geometries: An idealized modeling perspective. *J. Atmos. Sci.*, **61**, 588–606, [https://doi.org/10.1175/1520-0469\(2004\)061<0588:SOOPTC>2.0.CO;2](https://doi.org/10.1175/1520-0469(2004)061<0588:SOOPTC>2.0.CO;2).
- Comarazamy, D. E., and J. E. González, 2011: Regional long-term climate change (1950–2000) in the midtropical Atlantic and its impacts on the hydrological cycle of Puerto Rico. *J. Geophys. Res.*, **116**, D00Q05, <https://doi.org/10.1029/2010JD015414>.
- Couach, O., and Coauthors, 2003: An investigation of ozone and planetary boundary layer dynamics over the complex topography of Grenoble combining measurements and modeling. *Atmos. Chem. Phys.*, **3**, 549–562, <https://doi.org/10.5194/acp-3-549-2003>.
- Dawson, J. P., P. J. Adams, and S. N. Pandis, 2007: Sensitivity of ozone to summertime climate in the eastern USA: A modeling case study. *Atmos. Environ.*, **41**, 1494–1511, <https://doi.org/10.1016/j.atmosenv.2006.10.033>.
- De Wekker, S. F. J., and M. Kossmann, 2015: Convective boundary layer heights over mountainous terrain—A review of concepts. *Front. Earth Sci.*, **3**, 77, <https://doi.org/10.3389/feart.2015.00077>.
- Durre, I., C. N. Williams, X. Yin, and R. S. Vose, 2009: Radiosonde-based trends in precipitable water over the northern hemisphere: An update. *J. Geophys. Res.*, **114**, D05112, <https://doi.org/10.1029/2008JD010989>.
- Eresmaa, N., A. Karppinen, S. M. Joffe, J. Räsänen, and H. Talvitie, 2006: Mixing height determination by ceilometer. *Atmos. Chem. Phys.*, **6**, 1485–1493, <https://doi.org/10.5194/acp-6-1485-2006>.
- Erickson, L. E., G. L. Newmark, M. J. Higgins, and Z. Wang, 2020: Nitrogen oxides and ozone in urban air: A review of 50 plus years of progress. *Environ. Prog. Sustainable Energy*, **39**, e13484, <https://doi.org/10.1002/ep.13484>.
- Evan, A. T., C. Flamant, M. Gaetani, and F. Guichard, 2016: The past, present and future of African dust. *Nature*, **531**, 493–495, <https://doi.org/10.1038/nature17149>.
- Gentine, P., A. Massmann, B. R. Lintner, S. Hamed Alemohammad, R. Fu, J. K. Green, D. Kennedy, and J. Vilà-Guerau de Arellano, 2019: Land–atmosphere interactions in the tropics—A review. *Hydrol. Earth Syst. Sci.*, **23**, 4171–4197, <https://doi.org/10.5194/hess-23-4171-2019>.
- Giannini, A., Y. Kushnir, and M. A. Cane, 2000: Interannual variability of Caribbean rainfall, ENSO, and the Atlantic Ocean. *J. Climate*, **13**, 297–311, [https://doi.org/10.1175/1520-0442\(2000\)013<0297:IVOCRE>2.0.CO;2](https://doi.org/10.1175/1520-0442(2000)013<0297:IVOCRE>2.0.CO;2).
- Gioda, A., O. L. Mayol-Bracero, F. N. Scatena, K. C. Weathers, V. L. Mateus, and W. H. McDowell, 2013: Chemical constituents in clouds and rainwater in the Puerto Rican rainforest: Potential sources and seasonal drivers. *Atmos. Environ.*, **68**, 208–220, <https://doi.org/10.1016/j.atmosenv.2012.11.017>.
- González, G., M. R. Willig, and R. B. Waide, 2013: Ecological gradient analyses in a tropical landscape: Multiples perspectives and emerging themes. *Ecol. Bull.*, **54**, 13–20.
- , A. E. Van Beusekom, and C. R. Estrada, 2021: Luquillo experimental forest Sabana weather station scaffold tower 2018–2020 data. Forest Service Research Data Archive, accessed 18 March 2022, <https://doi.org/10.2737/RDS-2021-0030>.
- , —, and —, 2022: Luquillo experimental forest atmospheric and high and mid elevation weather data. Forest Service Research Data Archive, accessed 18 March 2022, <https://doi.org/10.2737/RDS-2022-0050>.
- Gouirand, I., M. R. Jury, and B. Sing, 2012: An analysis of low- and high-frequency summer climate variability around the Caribbean Antilles. *J. Climate*, **25**, 3942–3952, <https://doi.org/10.1175/JCLI-D-11-00269.1>.
- Gould, W. A., G. González, and G. Carrero Rivera, 2006: Structure and composition of vegetation along an elevational gradient in Puerto Rico. *J. Veg. Sci.*, **17**, 653–664, <https://doi.org/10.1111/j.1654-1103.2006.tb02489.x>.
- Haefelin, M., and Coauthors, 2012: Evaluation of mixing-height retrievals from automatic profiling lidars and ceilometers in view of future integrated networks in Europe. *Bound.-Layer Meteorol.*, **143**, 49–75, <https://doi.org/10.1007/s10546-011-9643-z>.
- Hall, T. C., A. M. Sealy, T. S. Stephenson, S. Kusunoki, M. A. Taylor, A. A. Chen, and A. Kitoh, 2013: Future climate of the Caribbean from a super-high-resolution atmospheric general circulation model. *Theor. Appl. Climatol.*, **113**, 271–287, <https://doi.org/10.1007/s00704-012-0779-7>.
- Hartigan, J. A., and M. A. Wong, 1979: A *k*-means clustering algorithm. *J. Roy. Stat. Soc.*, **28C**, 100–108, <https://doi.org/10.2307/2346830>.
- Jury, M. R., 2017: Caribbean air chemistry and dispersion conditions. *Atmosphere*, **8**, 151, <https://doi.org/10.3390/atmos8080151>.
- , 2020: Resolution-dependent perspectives on Caribbean hydro-climate change. *Hydrology*, **7**, 93, <https://doi.org/10.3390/hydrology7040093>.
- , and M. J. Santiago, 2010: Composite analysis of dust impacts on African easterly waves in the Moderate Resolution Imaging Spectrometer era. *J. Geophys. Res.*, **115**, D16213, <https://doi.org/10.1029/2009JD013612>.
- Karmalkar, A. V., M. A. Taylor, J. Campbell, T. Stephenson, M. New, A. Centella, A. Benzanilla, and J. Charlery, 2013: A review of observed and projected changes in climate for the islands in the Caribbean. *Atmósfera*, **26**, 283–309, [https://doi.org/10.1016/S0187-6236\(13\)71076-2](https://doi.org/10.1016/S0187-6236(13)71076-2).
- Ketterer, C., P. Zieger, N. Bukowiecki, M. C. Coen, O. Maier, D. Ruffieux, and E. Weingartner, 2014: Investigation of the planetary boundary layer in the Swiss Alps using remote sensing and in situ measurements. *Bound.-Layer Meteorol.*, **151**, 317–334, <https://doi.org/10.1007/s10546-013-9897-8>.
- Latha, R., B. Murthy, B. Sandeepan, V. Bhanage, A. Rathod, A. Tiwari, G. Beig, and S. Singh, 2021: Propagation of cloud base to higher levels during Covid-19-lockdown. *Sci. Total Environ.*, **759**, 144299, <https://doi.org/10.1016/j.scitotenv.2020.144299>.
- Lawton, R. O., U. S. Nair, R. A. Pielke, and R. M. Welch, 2001: Climatic impact of tropical lowland deforestation on nearby montane cloud forests. *Science*, **294**, 584–587, <https://doi.org/10.1126/science.1062459>.
- Liu, B., Y. Ma, W. Gong, M. Zhang, and J. Yang, 2019: Improved two-wavelength lidar algorithm for retrieving atmospheric boundary layer height. *J. Quant. Spectrosc. Radiat. Transfer*, **224**, 55–61, <https://doi.org/10.1016/j.jqsrt.2018.11.003>.

- Liu, Z., and Coauthors, 2009: The CALIPSO lidar cloud and aerosol discrimination: Version 2 algorithm and initial assessment of performance. *J. Atmos. Oceanic Technol.*, **26**, 1198–1213, <https://doi.org/10.1175/2009JTECHA1229.1>.
- Malkus, J. S., 1955: The effects of a large island upon the trade-wind air stream. *Quart. J. Roy. Meteor. Soc.*, **81**, 538–550, <https://doi.org/10.1002/qj.49708135003>.
- Martinuzzi, S., W. A. Gould, and O. M. R. González, 2007: Land development, land use, and urban sprawl in Puerto Rico integrating remote sensing and population census data. *Land-use Urban Plann.*, **79**, 288–297, <https://doi.org/10.1016/j.landurbplan.2006.02.014>.
- Miller, P. W., T. L. Mote, C. A. Ramseyer, A. E. Van Beusekom, M. A. Scholl, and G. González, 2018: A 42 year inference of cloud base height trends in the Luquillo Mountains of northeastern Puerto Rico. *Climate Res.*, **76**, 87–94, <https://doi.org/10.3354/cr01529>.
- , A. Kumar, T. L. Mote, F. D. S. Moraes, and D. R. Mishra, 2019: Persistent hydrological consequences of Hurricane Maria in Puerto Rico. *Geophys. Res. Lett.*, **46**, 1413–1422, <https://doi.org/10.1029/2018GL081591>.
- Mote, T. L., C. A. Ramseyer, and P. W. Miller, 2017: The Saharan air layer as an early rainfall season suppressant in the eastern Caribbean: The 2015 Puerto Rico drought. *J. Geophys. Res. Atmos.*, **122**, 10966–10982, <https://doi.org/10.1002/2017JD026911>.
- Mues, A., M. Rupakheti, C. Münkler, A. Lauer, H. Bozem, P. Hoor, T. Butler, and M. Lawrence, 2017: Investigation of the mixing layer height derived from ceilometer measurements in the Kathmandu Valley and implications for local air quality. *Atmos. Chem. Phys.*, **17**, 8157–8176, <https://doi.org/10.5194/acp-17-8157-2017>.
- Nadolski, V., 1998: Automated Surface Observing System (ASOS) user's guide. NOAA Doc., 74 pp., <https://www.weather.gov/media/asos/aum-toc.pdf>.
- Nair, U. S., R. O. Lawton, R. M. Welch, and R. A. Pielke, 2003: Impact of land use on Costa Rican tropical montane cloud forests: Sensitivity of cumulus cloud field characteristics to lowland deforestation. *J. Geophys. Res.*, **108**, 4206, <https://doi.org/10.1029/2001JD001135>.
- Nuijens, L., I. Serikov, L. Hirsch, K. Lonitz, and B. Stevens, 2014: The distribution and variability of low-level cloud in the North Atlantic trades. *Quart. J. Roy. Meteor. Soc.*, **140**, 2364–2374, <https://doi.org/10.1002/qj.2307>.
- Odum, H. T., and R. F. Pigeon, 1970: A tropical rain forest: A study of irradiation and ecology at El Verde, Puerto Rico. U.S. Atomic Energy Commission Division of Technical Information Rep., 1626 pp.
- Omar, A. H., and Coauthors, 2009: The CALIPSO automated aerosol classification and lidar ratio selection algorithm. *J. Atmos. Oceanic Technol.*, **26**, 1994–2014, <https://doi.org/10.1175/2009JTECHA1231.1>.
- Quan, J., and Coauthors, 2013: Evolution of planetary boundary layer under different weather conditions, and its impact on aerosol concentrations. *Particology*, **11**, 34–40, <https://doi.org/10.1016/j.partic.2012.04.005>.
- Ramanathan, V., R. Cess, E. Harrison, P. Minnis, B. Barkstrom, E. Ahmad, and D. Hartmann, 1989: Cloud-radiative forcing and climate: Results from the Earth radiation budget experiment. *Science*, **243**, 57–63, <https://doi.org/10.1126/science.243.4887.57>.
- Ray, D. K., U. S. Nair, R. O. Lawton, R. M. Welch, and R. A. Pielke, 2006: Impact of land use on Costa Rican tropical montane cloud forests: Sensitivity of orographic cloud formation to deforestation in the plains. *J. Geophys. Res.*, **111**, D02108, <https://doi.org/10.1029/2005JD006096>.
- Schwartz, N. B., A. M. Budsock, and M. Uriarte, 2019: Fragmentation, forest structure, and topography modulate impacts of drought in a tropical forest landscape. *Ecology*, **100**, e02677, <https://doi.org/10.1002/ecy.2677>.
- Seidel, D. J., C. O. Ao, and K. Li, 2010: Estimating climatological planetary boundary layer heights from radiosonde observations: Comparison of methods and uncertainty analysis. *J. Geophys. Res.*, **115**, D16113, <https://doi.org/10.1029/2009JD013680>.
- Shanley, J. B., M. Marvin-DiPasquale, O. Lane, W. Arendt, S. Hall, and W. H. McDowell, 2020: Resolving a paradox—High mercury deposition, but low bioaccumulation in northeastern Puerto Rico. *Ecotoxicology*, **29**, 1207–1220, <https://doi.org/10.1007/s10646-019-02108-z>.
- Singh, N., R. Solanki, N. Ojha, R. H. H. Janssen, A. Pozzer, and S. K. Dhaka, 2016: Boundary layer evolution over the central Himalayas from radio wind profiler and model simulations. *Atmos. Chem. Phys.*, **16**, 10559–10572, <https://doi.org/10.5194/acp-16-10559-2016>.
- Still, C. J., P. N. Foster, and S. H. Schneider, 1999: Simulating the effects of climate change on tropical montane cloud forests. *Nature*, **398**, 608–610, <https://doi.org/10.1038/19293>.
- Subramanian, R., and Coauthors, 2018: Air quality in Puerto Rico in the aftermath of Hurricane Maria: A case study on the use of lower cost air quality monitors. *ACS Earth Space Chem.*, **2**, 1179–1186, <https://doi.org/10.1021/acsearthspacechem.8b00079>.
- Taylor, M. A., F. S. Whyte, T. S. Stephenson, and J. D. Campbell, 2013: Why dry? Investigating the future evolution of the Caribbean low level jet to explain projected Caribbean drying. *Int. J. Climatol.*, **33**, 784–792, <https://doi.org/10.1002/joc.3461>.
- Torres-Delgado, E., D. Baumgardner, and O. L. Mayol-Bracero, 2021: Measurement report: Impact of African aerosol particles on cloud evolution in a tropical montane cloud forest in the Caribbean. *Atmos. Chem. Phys.*, **21**, 18011–18027, <https://doi.org/10.5194/acp-21-18011-2021>.
- Vaisala Oyj, 2010: Boundary Layer View Software BL-VIEW user's guide. Vaisala Doc., 63 pp.
- Van Beusekom, A. E., G. González, and M. M. Rivera, 2015: Short-term precipitation and temperature trends along an elevation gradient in northeastern Puerto Rico. *Earth Interact.*, **19**, <https://doi.org/10.1175/EI-D-14-0023.1>.
- , —, and M. A. Scholl, 2017: Analyzing cloud base at local and regional scales to understand tropical montane cloud forest vulnerability to climate change. *Atmos. Chem. Phys.*, **17**, 7245–7259, <https://doi.org/10.5194/acp-17-7245-2017>.
- , N. L. Álvarez-Berrios, W. A. Gould, M. Quiñones, and G. González, 2018: Hurricane Maria in the U.S. Caribbean: Disturbance forces, variation of effects, and implications for future storms. *Remote Sens.*, **10**, 1386, <https://doi.org/10.3390/rs10091386>.
- Velazquez-Lozada, A., J. E. Gonzalez, and A. Winter, 2006: Urban heat island effect analysis for San Juan, Puerto Rico. *Atmos. Environ.*, **40**, 1731–1741, <https://doi.org/10.1016/j.atmosenv.2005.09.074>.
- Venter, Z. S., K. Aunan, S. Chowdhury, and J. Lelieveld, 2020: COVID-19 lockdowns cause global air pollution declines. *Proc. Natl. Acad. Sci. USA*, **117**, 18984–18990, <https://doi.org/10.1073/pnas.2006853117>.
- Vingarzan, R., 2004: A review of surface ozone background levels and trends. *Atmos. Environ.*, **38**, 3431–3442, <https://doi.org/10.1016/j.atmosenv.2004.03.030>.

- Waide, R. B., and Coauthors, 2013: Climate variability at multiple spatial and temporal scales in the Luquillo Mountains, Puerto Rico. *Ecol. Bull.*, **54**, 21–41.
- Wang, H., C. A. S. Hall, F. N. Scatena, N. Fetcher, and W. Wu, 2003: Modeling the spatial and temporal variability in climate and primary productivity across the Luquillo Mountains, Puerto Rico. *For. Ecol. Manage.*, **179**, 69–94, [https://doi.org/10.1016/S0378-1127\(02\)00489-9](https://doi.org/10.1016/S0378-1127(02)00489-9).
- Willig, M. R., S. J. Presley, C. P. Bloch, I. Castro-Arellano, L. M. Cisneros, C. L. Higgins, and B. T. Klingbeil, 2011: Tropical metacommunities along elevational gradients: Effects of forest type and other environmental factors. *Oikos*, **120**, 1497–1508, <https://doi.org/10.1111/j.1600-0706.2011.19218.x>.
- Winker, D. M., M. A. Vaughan, A. Omar, Y. Hu, K. A. Powell, Z. Liu, W. H. Hunt, and S. A. Young, 2009: Overview of the CALIPSO Mission and CALIOP data processing algorithms. *J. Atmos. Oceanic Technol.*, **26**, 2310–2323, <https://doi.org/10.1175/2009JTECHA1281.1>.
- Wolff, G. T., D. F. Kahlbaum, and J. M. Heuss, 2013: The vanishing ozone weekday/weekend effect. *J. Air Waste Manage. Assoc.*, **63**, 292–299, <https://doi.org/10.1080/10962247.2012.749312>.
- Yoshida, K., M. Sugi, R. Mizuta, H. Murakami, and M. Ishii, 2017: Future changes in tropical cyclone activity in high-resolution large-ensemble simulations. *Geophys. Res. Lett.*, **44**, 9910–9917, <https://doi.org/10.1002/2017GL075058>.